Inter-compartment interaction in multi-impeller mixing
Part I. Experiments and multiple reference frame CFD

Haringa, Cees; Vandewijer, Ruben; Mudde, Robert F.

DOI
10.1016/j.cherd.2018.06.005

Publication date
2018

Document Version
Final published version

Published in
Chemical Engineering Research and Design

Contents lists available at ScienceDirect

Chemical Engineering Research and Design

journal homepage: www.elsevier.com/locate/cherd

Inter-compartment interaction in multi-impeller mixing: Part I. Experiments and multiple reference frame CFD

Cees Haringa[*], *Ruben Vandewijer*, *Robert F. Mudde*[1]

Transport Phenomena, Department of Chemical Engineering, Delft University of Technology, van der Maasweg 9, 2629HZ Delft, the Netherlands

ARTICLE INFO

Article history:
Received 19 November 2017
Received in revised form 24 April 2018
Accepted 1 June 2018
Available online 15 June 2018

MSC:
00-01
99-00 *Keywords:*
Mixing
Schmidt number
CFD
Multiple impellers
Macro instability

ABSTRACT

CFD simulations of mixing in single-phase multi-Rushton stirred tanks based on the RANS methodology frequently show an over-prediction of the mixing time. This hints at an under-prediction of the mass exchange between the compartments formed around the individual impellers. Some studies recommend tuning the turbulent Schmidt number to address this issue, but this appears to be an ad-hoc correction rather than physical adjustment, thereby compromising the predictive value of the method. In this work, we study the flow profile in between two Rushton impellers in stirred tank. The data hints at the presence of macro-instabilities, and a peak in turbulent kinetic energy in the region of convergent flow, which both may promote inter-compartment mass exchange. CFD studies using the steady-state multiple reference frame model (unsteady simulations are treated in part II) inherently fail to include the macro-instability, and underestimate the turbulent kinetic energy, thereby strongly over-estimating mixing time. Furthermore, the results are highly mesh-sensitive, with increasing mesh density leading to a poorer prediction of the mixing time. Despite proper results for 1-impeller studies, we do not deem MRF-RANS models suitable for mixing studies in multi-impeller geometries.

1. Introduction

Computational fluid dynamics (CFD) simulations offer a relatively cheap and fast approach towards evaluating the mixing performance of a range of impeller configurations, without the need of a lengthy experimental campaign. This requires that CFD simulations sufficiently capture the true mixing behavior, which gave rise to a significant body of validation literature. A review of literature focusing on single phase flows with Rushton turbines (Section 2) shows that Reynolds Averaged Navier Stokes (RANS) simulations yield decent results for single-impeller geometries (Coroneo et al., 2011), but appear to consistently overestimate mixing times in multi-impeller geometries (Montante et al., 2005; Moštěk et al., 2005; Kukuková et al., 2005; Jahoda et al., 2007); this over-estimation may hold for other impeller types at large spacing (Montante et al., 2005). Large Eddy simulations (LES) appear to adequately capture mixing behavior, but the required computation time prohibits routine application. We assess this overestimation of the mixing time in Rushton-stirred tanks with large impeller spacing by RANS simulations. Our original hypothesis was that of RANS simulations under-estimating μ_t in the

Abbreviations: MI, macro-instability; CoM, coefficient of mixing; LDA, laser Doppler anemometry; PIV, particle image velocimetry; RANS, Reynolds averaged Navier Stokes; MRF, multiple reference frames; SM, sliding mesh; (S/R)KE, standard/realizable $k-\epsilon$; RSM, Reynolds stress model; (D/L)ES, detached/large Eddy simulation.

[*] *Corresponding author.*
E-mail address: r.f.mudde@tudelft.nl (C. Haringa).
[1] Current address: DSM Biotechnology Center, Alexander Fleminglaan 1, 2613AX Delft, the Netherlands.

https://doi.org/10.1016/j.cherd.2018.06.005
0263-8762/

Nomenclature

Roman

a_n	damping coefficient, Eq. (3), –
C_t	tracer concentration, kg/m^3
C	off-bottom clearance impeller, m
c_n	strength coefficient, Eq. (3), –
ΔC	inter-impeller clearance, m
D	impeller diameter, m
D	diffusion coefficient, m^2/s
D_t	diffusion coefficient, turbulent, m^2/s
E_p/E_t	fraction of periodic energy in spectrum of u', –
f	frequency, s^{-1}
$f_{1.1}$	base frequency 1, s^{-1}
$f_{2.1}$	base frequency 2, s^{-1}
$f_{1.2}$	harmonic frequency 1, s^{-1}
$f_{2.2}$	harmonic frequency 2, s^{-1}
F_Q	pumping number, –
h	axial coordinate, m
H	tank height, m
k	slot number (autocorrelation), –
k_t	turbulent kinetic energy, m^2/s^2
k_{MI}	macro-instability kinetic energy, m^2/s^2
$k_{t,*}$	$k_t + k_{MI}$, m^2/s^2
$k_{t,fit}$	k_t computed via auto-correlation fit, m^2/s^2
$k_{t,SI}$	k_t computed via spectral integration, m^2/s^2
$k_{MI,fit}$	k_{MI} computed via auto-correlation fit, m^2/s^2
$k_{MI,SI}$	k_{MI} computed via spectral integration, m^2/s^2
N	impeller revolutions, 1/s
N_c	no. gridcells, –
Q_{ax}	axial flow rate, L/s
r	radial position, m
R	tank radius, m
Sc_t	turbulent Schmidt number, –
T	tank diameter, m
Δt	timestep size, s
u'	fluctuating velocity, m/s
U	mean velocity, m/s
U_{tip}	impeller tip speed, m/s
V	tank volume, m^3
V_i	grid cell volume, m^3
w	Tukey–Hanning window, –

Greek

λ	laser wavelength, nm
μ	viscosity, dynamic, Pa s
μ_t	viscosity, dynamic, turbulent, Pa s
ϵ	turbulent dissipation rate, m^2 s^3
$\hat{\rho}$	auto-correlation coefficient, –
ρ_l	density, kg/m^3
τ_{lag}	lag time, s
Ψ	noise component, –
τ_{95}	mixing time, s
θ_{95}	mixing number, $N \cdot \tau_{95}$ –

horizontal plane segregating the compartments formed around the individual impellers, hence under-estimating mass exchange between them. During our investigation, we additionally observed a macro-instability in the inter-compartment region, which significantly contributed to mass exchange. In several prior publications, inter-compartment mass exchange was boosted by tuning of the turbulent Schmidt number, $Sc_t = \nu_t/(D_t)$ (Montante et al., 2005; Gunyol et al., 2009; Haringa et al., 2016). We pose that this tuning is not based on physical reasoning. Instead, it is a patchwork solution covering exchange by virtue of the macro-instability, as well as under-predicted turbulent exchange, as Tominaga and Stathopoulos (2007) similarly discussed for mispredicted scalar spreading in jets. Such an ad-hoc correction compromises the predictive capabilities of RANS-based stirred tank simulations. Whereas other publications on multi-impeller mixing focused primarily on overall mixing behavior, we study the flow in region *between* the impellers in detail, using a combination of Laser Doppler Anemometry (LDA) experiments, RANS and LES simulations. We combine these results with both steady and unsteady CFD simulations, to answer as to why RANS simulations poorly capture mixing in multi-impeller tanks. In this first part of the work, we focus on the experimental assessment and steady RANS simulations, unsteady simulations including LES are considered in part two.

2. Literature overview: RANS simulations of Rushton turbines

In this literature overview, we discuss the use of RANS simulations to study mixing in vessels stirred with Rusthon turbines. LES and DES models are the subject of part II of this work.

2.1. *The impeller discharge stream*

Most hydrodynamic research in stirred tanks focused on the impeller discharge stream and trailing vortices, being the regions where much of the hydrodynamic action happens. Experiments typically measured the turbulent kinetic energy (k_t) and discharge stream velocity by LDA (Wu and Patterson, 1989; Ng et al., 1998; Ng and Yianneskis, 2000; Murthy and Joshi, 2008; Schäfer et al., 1997; Venneker et al., 2010; Lee and Yianneskis, 1998; Derksen et al., 1999) or particle image velocimetry (PIV) (Khopkar et al., 2004; Ranade et al., 2001; Escudié and Liné, 2003; Escudié et al., 2004; Huchet et al., 2009; Baldi and Yianneskis, 2004; Baldi et al., 2004; Ducci and Yianneskis, 2005; Liné et al., 2013). Early studies typically computed the turbulent dissipation rate ϵ on dimensional grounds (Wu and Patterson, 1989), or via the energy balance (Escudié and Liné, 2003; Escudié et al., 2004). Direct ϵ measurements have been conducted with high-resolution LDA and PIV (Huchet et al., 2009; Baldi and Yianneskis, 2004; Baldi et al., 2004; Ducci and Yianneskis, 2005). These show that estimations of ϵ from dimensional analysis are reasonable in the bulk, but underestimate ϵ close to the blade, where turbulence is strongly anisotropic (Hartmann et al., 2004). The bulk of CFD studies report consensus regarding the impeller discharge velocity (Gunyol and Mudde, 2009; Ng et al., 1998; Zakrzewska and Jaworski, 2004; Ammar et al., 2011; Lane et al., 2000; Brucato et al., 1998; Jenne and Reuss, 1999), while turbulence parameters yield less universal agreement. Brucato et al. (1998) underestimated k_t using the standard $k-\epsilon$ (SKE) model, using inner–outer (IO) and sliding mesh (SM) impeller modeling. Gunyol and Mudde (2009) reported poor agreement using RNG–KE but found good results for k_t with SKE and the realizable $k-\epsilon$ (RKE) models, with multiple-reference frame (MRF) impeller modeling. The Reynolds stress model (RSM) compared less favorably, but outperformed RNG–KE. Singh et al. (2011) noted k_t in the discharge stream is reasonably well predicted using SM–SKE, although near the blade performance is

poorer, with the trailing vortices being too small, and inward-curved compared to experimental data (Derksen et al., 1999; Ranade et al., 2001; Escudié et al., 2004). Underestimations in ϵ of up to 50% were reported by Ng et al. (1998), Ng and Yianneskis (2000), who modeled the full 3D impeller geometry. With 1–3 cells across the blade thickness, poorly resolved flow around the blade may cause this underestimation. Studies using sheet-body impellers and baffles performed better (Gunyol and Mudde, 2009; Coroneo et al., 2011; Singh et al., 2011), although high mesh densities (10^6+ cells for a one impeller, 360° domain) are required for mesh independent results (Coroneo et al., 2011). For these, results for both the SKE and RKE model agree well with the dimensional assessment of ϵ by Wu and Patterson (Gunyol and Mudde, 2009). This is unsurprising, as the $k-\epsilon$ method is built largely on the same assumptions (isotropy and a single turbulent length-scale $L_{res} = Ak_t^{3/2}/\epsilon$). Singh et al. (2011) (SM–SKE) showed that the agreement in ϵ breaks down near the blade when compared to direct ϵ measurements. Further away from the impeller, where the $k-\epsilon$ model assumptions reasonably hold (Hartmann et al., 2004), decent agreement in ϵ was observed by Singh et al.

2.2. *Mixing in Rushton-stirred tanks*

2.2.1. *Definition of mixing time*

We report the 95% mixing time in dimensionless form; $\theta_{95} = N \cdot \tau_{95}$ with τ_{95} the mixing time in s and N the agitation rate in s^{-1}. For point-measurements we consider τ_{95} as the time where the normalized tracer concentration $C_t/\bar{C}_t$ is between 0.95 and 1.05 ($\bar{C}_t$ the vessel average) (Kukuková et al., 2005; Jahoda et al., 2007; Bujalski et al., 2002a,b,c; Jaworski et al., 2000a,b; Magelli et al., 2013). Probes have the advantage of recording dynamics that are directly comparable to CFD simulations, but the results may be location specific, and invasive probes may disturb the local flow. The coefficient of mixing (CoM) (Kukuková et al., 2008; Kukukova et al., 2009; Hartmann et al., 2006) (alternatively called Coefficient of Variation (CoV)) is used to quantify τ_{95} based on CFD field data. As CFD meshes are typically non-uniform, volume-weighing should be applied in the determination of the CoM (Hartmann et al., 2006):

$$\mathrm{CoM} = \sqrt{\left(\frac{\Sigma_i \left(\frac{C_{t,i}-\bar{C}_t}{\bar{C}_t}\right)^2 \Delta V_i}{\Sigma_i \Delta V_i}\right)} \quad (1)$$

Kukuková et al. (2008) set CoM = 0.05 as the 95% mixing limit, while Hartmann et al. (2006) report CoM = 0.0283 as 95% of the volume being 95% mixed, based on numerical experiments. We apply the limit of Hartmann, but do not consider either indicator to be superior provided consistency is applied. Coroneo et al. (2011) also used the CoM to quantify mixing by plane laser induced fluorescence (P-LIF). Some studies with alternative mixing indicators are found in literature, such as 95% of the volume being decolored (Moo-Young et al., 1972). Lee and Yianneskis (1997) suspended thermally sensitive liquid-crystal particles and applied a heat pulse, measuring θ_{95} when 95% of the particles had the same hue.

2.2.2. *Single impeller systems*

The mixing time correlation of Yeoh et al. (2005) yields $\theta_{95} = 30.7$ for a single Rushton turbine, with $D = T/3$, $H = T$. The Ruszkowski–Grenville correlation (Yeoh et al., 2005), valid for various impeller types (Nienow, 1997), predicts $\theta_{95} = 27.5$. Typical experimental and CFD results give $\theta_{95} \approx 30$–40 (Table 1), showing the correlations are reasonable. There is quite some variation in the results however. In experiments, this may be due to probe location (Raghav Rao and Joshi, 1988; Kukuková et al., 2005; Jahoda et al., 2007), or due to different methods used to quantify the mixing time (Lee and Yianneskis, 1997; Moo-Young et al., 1972), that are not mutually comparable. Similar observations can be made for the CFD results. LES methods – discussed in more detail in part II – generally perform well, but different mixing quantification methods yield different results. Especially 3D-CoM (Hartmann et al., 2006)) yields a higher τ_{95}, as it considers the entire volume, including poorly mixed regions. This calls caution when comparing mixing times between different studies, experimental or numerical. Focusing on RANS methods, sliding mesh simulations were reported to over-predict θ_{95} (Jahoda et al., 2007; Zadghaffari et al., 2010). In contrast, the MRF–SKE approach of Jahoda et al. and Kukukova et al. underestimated θ_{95} compared with their measurements. The agreement between experimental probe measurements and non-invasive LIF measurements (Distelhoff et al., 1997; Javed et al., 2006) makes it unlikely these differences are due to the probe influencing flow. More likely, the mesh resolution was insufficient. Results by Coroneo et al. (different geometry: $D = T/3$, $C = T/2$, $H = T$) do show good agreement between PLIF data and MRF–SKE simulations (2D-CoM) qualitatively and quantitatively. Their mesh of 2000k cells was much finer than used in other MRF studies. Coroneo et al. found the discharge velocity profile and torque-based power number Po_τ, often used for mesh dependency studies, are rather insensitive to mesh details (Coroneo et al., 2011). The dissipation based power number Po_ϵ is more sensitive, and in better agreement with the mesh sensitivity of θ_{95}.

2.2.3. *Multi-impeller systems*

The flow in multi-impeller systems depends strongly on the inter-impeller clearance (Rutherford et al., 1996). We focus on Rushton-stirred systems with a spacing $\Delta C = T$, which exhibit parallel flow (Mishra and Joshi, 1994; Rutherford et al., 1996), forming separate compartments around the individual impellers. We refer to the region where these compartments meet as the inter-compartment region. with the exact horizontal separation between the compartments referred to as the inter-compartment plane. In this plane, the mean flow is dominantly radial, and little mass exchange between the compartments is expected by the *mean* convective flow. This forms a rate-limiting step in mixing; comparing the experimental θ_{95} between 1-, 2- and 4 impeller systems (Table 1–3, respectively) shows θ_{95} more than doubles upon doubling the number of impellers. All summarized multi-impeller studies report θ_{95} based on invasive probes, with tracer injected at the vessel top. In case of multiple probes, the bottom probe reading is reported, giving the highest θ_{95}. Early studies by Jaworski et al. (2000a,b) and Bujalski et al. (2002a,c), with very limited mesh resolution, reported up to a factor 2 overestimation of θ_{95}, both with SM–SKE and MRF–SKE. Kukuková et al. (2005) reported an 8.6% over-estimation for MRF–SKE, while Jahoda et al. (2007) observed 20% and 26% over-estimations for MRF–SKE and SM–SKE, respectively. The LES simulations of Jahoda et al. (2007) showed highly similar probe dynamics compared to their experiments; the higher degree of noise in experimental data did in an 11.4% under-estimation of θ_{95}. Only MRF–SKE simulations are reported for 3- and 4-

Table 1 – An overview of mixing times for a single impeller geometry ($D = T/3$, $C = T/3$, $H = T$): experimental (t_{95}). Measure indicates the method used to quantify τ_{95}: x-P: x probes, T: thermal, C: decolorization, 3D-CoM: coefficient of mixing, volume. MM: min–max method.

Author	θ_{95}	Measure	Re	Method	Sc_t	Mesh	Ref.
Kukukova et al.	33	1-P	46,667	Conductivity	–	–	(Kukuková et al., 2005)
Jahoda et al.	34	1-P	46,667	Conductivity	–	–	(Jahoda et al., 2007)
Lee et al.	21.6	T	40,000	Thermal	–	–	(Lee and Yianneskis, 1997)
Distelhoff et al	36	8-P	24,000	LIF	–	–	(Distelhoff et al., 1997)
Javed et al	32	32-P	24,000	LIF	–	–	(Javed et al., 2006)
Moo-Young et al.	36	C	24,000	Decolorization	–	–	(Moo-Young et al., 1972)
Raghav Rao et al.	48.2 (avg.)	1-P	>100,000	Conductivity	–	–	(Raghav Rao and Joshi, 1988)
Rewatkar et al.	39.5 (avg.)	1-P	>200,000	Conductivity	–	–	(Rewatkar and Joshi, 1991)
Nere et al.	35.3	MM	46,722	B. C. $k-\epsilon$	Not reported	280k	(Nere et al., 2003)
Kukukova et al.	23.5	1-P	46,722	MRF $k-\epsilon$	0.7	330k	(Kukuková et al., 2005)
Jahoda et al.	13.5	1-P	46,722	MRF $k-\epsilon$	0.7	615k	(Jahoda et al., 2007)
Jahoda et al.	50	1-P	46,722	SM $k-\epsilon$	0.7	615k	(Jahoda et al., 2007)
Javed et al	27	32-P	24,000	SM $k-\epsilon$	0.7	112k	(Javed et al., 2006)
Zadghaffari et al	40–80	1-P	41,667	SM LES	0.7	971k	(Zadghaffari et al., 2010)
Jahoda et al.	26	1-P	46,722	SM–LES	0.7	615k	(Jahoda et al., 2007)
Yeoh et al.	33.2	48-P	4000	SM–LES	0.7	330k	(Yeoh et al., 2005)
Hartmann et al.	39.8–54.7	3D-CoM	24,000	SM–LES	0.7	13,824k	(Hartmann et al., 2006)

Table 2 – An overview of mixing results with 2 impeller geometries: CFD and experimental data. Unless otherwise stated, $D = T/3$ and $\Delta C = T$. All mixing time measurements were probe-based. For turbulent Schmidt number Sc_t, n.r. = not reported.

Author	*Geometry*	θ_{95}	Re	Method	Sc_t	Mesh	Ref.
Kukukova et al.	$C = T/3$	104.5	46,722	Conductivity	–	–	(Kukuková et al., 2005)
Kukukova et al.	$C = T/3$	113.5	46,722	MRF $k-\epsilon$	0.7	286k	(Kukuková et al., 2005)
Jahoda et al.	$C = T/3$	92	46,722	Conductivity	0.7	–	(Jahoda et al., 2007)
Jahoda et al.	$C = T/3$	110	46,722	MRF $k-\epsilon$	0.7	1230k	(Jahoda et al., 2007)
Jahoda et al.	$C = T/3$	116	46,722	SM $k-\epsilon$	0.7	1230k	(Jahoda et al., 2007)
Jahoda et al.	$C = T/3$	81.5	46,722	SM LES	0.7	1230k	(Jahoda et al., 2007)
Jaworski et al.	$C = T/4$, $D = T/2$	46.6	162,000	Conductivity	–	–	(Jaworski et al., 2000a,b)
Jaworski et al.	$C = T/4$, $D = T/2$	48.9	216,000	Conductivity	–	–	(Jaworski et al., 2000a,b)
Jaworski et al.	$C = T/4$, $D = T/2$	137.5	162,000	SM $k-\epsilon$	n.r.	70k/180°	(Jaworski et al., 2000a,b)
Jaworski et al.	$C = T/4$, $D = T/2$	125.2	216,000	SM $k-\epsilon$	n.r.	70k/180°	(Jaworski et al., 2000a,b)
Jaworski et al.	$C = T/4$, $D = T/2$	140	324,000	SM $k-\epsilon$	n.r.	70k/180°	(Jaworski et al., 2000a,b)
Bujalski et al.	$C = T/4$, $D = T/2$	176	216,000	MRF $k-\epsilon$	n.r.	115k	(Bujalski et al., 2002a,c)

Table 3 – An overview of mixing results for 3 and 4 impeller geometries. In all cases, $H = n \cdot T$ where n is the number of impellers, $\Delta C = T$ and $D = T/3$.

Author	*Geometry*	θ_{95}	Re	Method	Sc_t	Mesh	Ref.
Jahoda et al.	3 *Imp*., $C = T/2$	197	21,000	Conductivity	–	–	(Jahoda and Machon, 1994)
Jahoda et al.	3 *Imp*., $C = T/2$	186	25,210	Conductivity	–	–	(Jahoda and Machon, 1994)
Jahoda et al.	3 *Imp*., $C = T/2$	212	33,610	Conductivity	–	–	(Jahoda and Machon, 1994)
Jahoda et al.	3 *Imp*., $C = T/2$	210	42,015	Conductivity	–	–	(Jahoda and Machon, 1994)
Jahoda et al.	3 *Imp*., $C = T/2$	204	50,415	Conductivity	–	–	(Jahoda and Machon, 1994)
Mostek et al.	3 *Imp*., $C = T/2$	239	46,722	Conductivity	–	–	(Moštěk et al., 2005)
Mostek et al.	3 *Imp*., $C = T/2$	286	46,722	MRF $k-\epsilon$	0.7	1537k	(Moštěk et al., 2005)
Mostek et al.	3 *Imp*., $C = T/3$	236	46,722	Conductivity	–	–	(Moštěk et al., 2005)
Mostek et al.	3 *Imp*., $C = T/3$	273	46,722	MRF $k-\epsilon$	0.7	1537k	(Moštěk et al., 2005)
Jahoda et al., 1994	4 *Imp*., $C = T/2$	400	21,000	Conductivity	–	–	(Jahoda and Machon, 1994)
Jahoda et al., 1994	4 *Imp*., $C = T/2$	387	25,210	Conductivity	–	–	(Jahoda and Machon, 1994)
Jahoda et al., 1994	4 *Imp*., $C = T/2$	392	33,610	Conductivity	–	–	(Jahoda and Machon, 1994)
Jahoda et al., 1994	4 *Imp*., $C = T/2$	405	420,15	Conductivity	–	–	(Jahoda and Machon, 1994)
Jahoda et al., 1994	4 *Imp*., $C = T/2$	402	50,415	Conductivity	–	–	(Jahoda and Machon, 1994)
Montante et al.	4 *Imp*., $C = T/2$	461	37,500	Conductivity	–	–	(Montante et al., 2005)
Mostek et al.	4 *Imp*., $C = T/2$	437	46,722	Conductivity	–	–	(Moštěk et al., 2005)
Montante et al.	4 *Imp*., $C = T/2$	476	37,500	SM $k-\epsilon$	0.1	350k	(Montante et al., 2005)
Mostek et al.	4 *Imp*., $C = T/2$	466	46,722	MRF $k-\epsilon$	0.7	1984k	(Moštěk et al., 2005)
Mostek et al.	4 *Imp*., $C = T/3$	439	46,722	Conductivity	–	–	(Moštěk et al., 2005)
Mostek et al.	4 *Imp*., $C = T/3$	477	37,500	MRF $k-\epsilon$	0.7	1984k	(Moštěk et al., 2005)

impeller systems. Montante et al. required a strongly lower turbulent Schmidt number, $Sc_t = 0.1$ (Montante et al., 2005), to yield agreement with experiments in a 4 impeller tank; similar observations were made in other studies (Delafosse et al., 2014; Gunyol et al., 2009). Moštěk et al. (2005) did not tune Sc_t, and reported an approximately 20% overestimation in θ_{95} compared to their measurements with 3 impellers (40% compared to Jahoda and Machon (1994)). They found decent agreement in 4 impeller systems compared to their own measurements (they did over-estimate θ_{95} compared to Jahoda and Machon (1994)). An important observation in the work of Mostek et al. for 3 and 4 impellers, is that increasing mesh density led to an increase in θ_{95}, with mesh independence not yet reached at the finest meshes. The number of gridcells in all multi-impeller studies reported above was lower than in the single-impeller study of Coroneo et al. (2011), implying that further refinement may lead to a considerably stronger over-estimation of θ_{95} in multi-impeller systems; the decent results of Mostek et al. for 4 impellers may be due to insufficient resolution, rather than inherently good model performance. Hydro-dynamically, the inter-compartment region is under-studied; studies typically focus on the impeller discharge stream rather than the quiescent bulk region (Delafosse et al., 2014). Micale et al. (1999) reported a small peak in k_t in the inter-compartment region with LDA data, possibly due to the generation of turbulent kinetic energy by the colliding circulation loops. This turbulence may enhance mixing across the inter-compartment plane, and hence deserves more attention: it may be an underestimation of turbulence in the compartment segre region leads to poor mixing predictions with RANS models, masked by the effects of insufficient mesh resolution.

A second phenomenon that may impact inter-compartment mixing is the presence of Macro-instabilities (MIs). These have been extensively studied in single-impeller geometries, both experimentally and numerically (Roussinova et al., 2003; Hartmann et al., 2004; Nikiforaki et al., 2004). Nikiforaki et al. (2003) suggest jet instabilities or instabilities by precessing vortices are the dominant cause. Paglianti et al. (2006, 2008) report both these effects are present in Rushton-stirred tanks. As for both phenomena frequency f scales linear with agitation rate N, MI frequencies are reported here in f/N. In the discharge stream of a 2 impeller system, frequencies of $f/N \approx 0.02$ and $f/N \approx 0.055$ are found for precessing vortices and jet instabilities, respectively (Paglianti et al., 2008). Guillard et al. similarly identified instabilities with $f/N \approx 0.05 - 0.08$ in the region above the top impeller (Guillard et al., 2000a,b). If these macro-oscillations lead to oscillations in the inter-compartment plane, they may promote mixing between the compartments. By construction, frozen-flowfield MRF simulations are not able to capture these oscillations.

2.3. Hypothesis

No consistent under- or over-estimation in θ_{95} is observed for RANS simulations with 1 impeller, and Coroneo et al. (2011) showed quantitative and qualitative agreement in mixing behavior can be obtained with MRF–SKE, given sufficient mesh resolution. In contrast, multi-Rushton RANS-CFD studies show a consistent over-prediction of θ_{95}, which in case of MRF simulation worsens with increasing mesh resolution. This hints that the overestimation of θ_{95} in such systems originates from poor assessment inter-compartment exchange, while intra-compartment can be properly captured. In the inter-compartment plane, the flow is dominantly parallel meaning that turbulence and/or MIs control mass transport between the compartments. In line with Jaworski et al. (2000b), we hence pose the hypothesis that RANS models inherently over-estimate θ_{95} by (a) an under-prediction of μ_t due to incorrect assessment of turbulence in the parallel flow region and/or (b) failing to capture the effect of MIs on inter-compartment mixing.

Table 4 – Meshes used in this work. 2IF represents a 360° domain and 2IP represents the 60° domain. The last letter(s) represent the mesh quality (C = crude, M = medium, F = fine, SF = super-fine). N_c is the number of gridcells.

Name	N_c	Domain	Methods
2IP-C	94k	60°	RKE, RSM
2IP-M	506k	60°	RKE, RSM
2IP-F	812k	60°	RKE, RSM, SM-RKE
2IF-C	648k	360°	RKE, RSM, SM-RKE, LES
2IF-M	1997k	360°	RKE, RSM, SM-RKE, SM-RSM, LES
2IF-F	5884k	360°	RKE, RSM, SM-RKE
2IF-SF	10,584k	360°	RKE, RSM, LES

3. Materials and methods

3.1. CFD setup

We focus on the realizable $k-\epsilon$ (RKE) and Reynolds stress model (RSM) with linear-pressure strain formulation. These models are well established in stirred tank modeling; a summary can be found in Gunyol and Mudde (2009), for example. A 2-impeller stirred tank with height $H = 2T$, impeller diameter $D = T/3$, off-bottom clearance $C = T/3$ and impeller clearance $\Delta C = T$ was modeled. Here, tank diameter $T = 0.29$ m, as used by Jahoda et al. (2007). The tank contains 4 baffles with width $T/10$. All internals were modeled as sheet bodies (Gunyol and Mudde, 2009; Coroneo et al., 2011). Both a 360° domain and 60° domain were modeled to assess the influence of a symmetry assumption (Gunyol and Mudde, 2009; Gunyol et al., 2009; Haringa et al., 2016, 2017). Using a 60° section introduces 6 baffles; the effect of this additional baffling was found to be small (Gunyol and Mudde, 2009). As in Jahoda et al. (2007), the bottom tracer concentration probe is placed at $T/4$ from the bottom, between the baffles, at $T/20$ from the wall. The top probe is placed at $1.25T$, at the same radial and angular position. The agitation rate is set to $N = 5\ s^{-1}$. In order to use the MRF method, the domain is separated in a stationary zone, and rotating zones around the individual impellers. These rotating zones do not overlap with the inter-compartment plane. Structured hexahedral meshes were used; the grid sizes N_c are reported in Table 4, with the 2IF series being the full domain, and the 2IP series representing a 60° slice. Mesh details are further specified in Supplementary material B. Spatial discretization was set to 2nd order upwind (Gunyol and Mudde, 2009; Coroneo et al., 2011) and standard wall functions were employed. The vessel top was set to no-shear to mimic a free surface, all other walls were no-slip. Convergence was declared when the residuals $<10^{-5}$ and the mean velocity remained within 0.1% over 1000 iterations. The velocity and turbulence fields were frozen during mixing. Tracer was introduced as a pas-

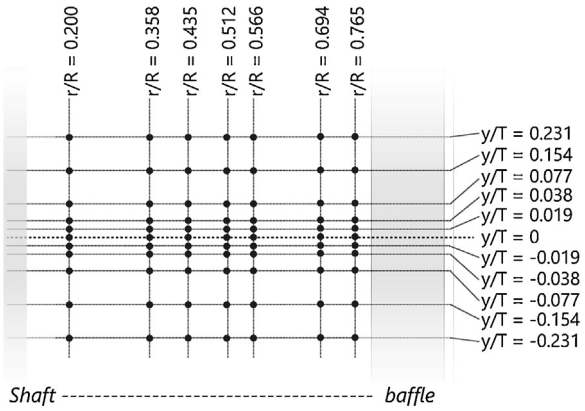

Fig. 1 – Measurement grid for the LDA-experiments in the mid-compartment plane. Axial positions given are non-dimensionalized with the tank diameter T, radial with tank radius R = D/2. y = 0 is the central position between the impeller (the most likely location of the inter-compartment plane), at height 5T/6 from the bottom, and r = 0 the impeller shaft.

sive scalar in a spherical volume (with a radius of 0.0125 m), at height $h = 0.551$ m from the bottom, at $r = 0.0725$ m, in the baffle plane. A timestep size of $\Delta t = 0.005$ s was used with second order implicit time discretization. The tracer and bulk fluid had equal properties, $\rho = 1000\,kg/m^3$ and $\mu = 0.001$Pa s, such that the tracer will not disturb the flowfield. The FLUENT default simple gradient diffusion hypothesis (SGDH) was used to determine turbulent scalar diffusion, modeling the diffusive flux as $J_i = -(\rho_l D + \mu_t/Sc_t)\nabla C_t$ with $D = 10^{-9}$ m^2/s the molecular diffusion coefficient, μ_t the turbulent viscosity, C_t the scalar concentration. $Sc_t = 0.7$ is the turbulent Schmidt number. An unpublished simulation with the generalized gradient diffusion hypothesis (GGDH) yielded no significant change in θ_{95}, both for RKE and RSM simulations.

The axial flowrate Q_{ax} through the mid-impeller plane ($y = 0$ in Fig. 1) was computed by iso-clipping this surface, retaining only locations with $u_{ax} < 0$ (downward flow), and reporting the total mass-flowrate through the remaining faces in FLUENT. Due to mass conservation, an equal value was found when iso-clipping to retain only upward flow.

3.2. LDA setup

We used a 2-probe TSI powersight laser system (150 mW) with $\lambda_1 = 561$ nm (axial) and $\lambda_2 = 532$ nm (radial), operated in backward scattering mode. A glass tank ($T = 0.26$ m, $H = 2T$, $C = T/3$, $\Delta C = T$, 4 aluminum baffles of $T/10$) was placed in a water-filled rectangular glass box for refractive index matching. Two standard Rushton turbines were mounted on a centered shaft of diameter $d_s = 0.02$ m. A graphical layout of the setup is given in Supplementary material A. The experiments reported in this work were conducted after the CFD simulations. Due to the equipment available in our lab, the experimental tank diameter is slightly smaller than the diameter used in CFD simulations. All geometric ratios are equal, however. The experiments were conducted at $N = 5.78\,s^{-1}$ due to limitations of the motor, giving $Re = 4.34 \times 10^4$, compared to 4.67×10^4 (at $N = 5.0\,s^{-1}$) by Jahoda et al. (2007) and in our CFD work. We do not expect these differences to influence the results, as both simulations and experiments are conducted in the fully turbulent regime, and results are presented in dimensionless form. Hollow glass seeding ($d_p = 8$–$12\,\mu$m, Stokes number $St \approx 0.03$) was used.

Verification measurements were conducted in the impeller outflow at 6 radial positions ($r = [50, 60, 70, 77, 90, 102]$ mm), at the height of the impeller disc of both impellers, in the baffle plane. The average data rate was 340–500 Hz (axial) and 830–850 Hz (radial). Data in the inter-compartment region was recorded at 7 radial and 11 axial positions, which are specified in Fig. 1, with $y = 0$ located at height 5T/6, measured from the bottom. Each measurement 50,000 datapoints were collected, measurements were done in 5-fold. The average data rates were 289 Hz (axial) and 343 Hz (radial). These are insufficient to resolve the full turbulence spectrum, but suffice to measure the energy-carrying motions which are expected to be relevant for inter-compartment mass exchange.

3.2.1. Data processing

LDA data processing was conducted in MATLAB 8.6.0. The setup contained a burst counter to remove false registrations, the velocity bias was corrected using gate-time weighing. The mean velocity is retrieved by time-averaging the velocity signal; subtracting the mean yields the fluctuating velocity. The contribution of noise and periodic flow components were assessed via the slotted auto-correlation method with local variance normalization (Tummers and Passchier, 1772c; van Maanen et al., 1999), with the auto-correlation $\hat{\rho}$ computed as:

$$\hat{\rho}(k\Delta\tau_{lag}) = \frac{\Sigma u'(t_i)u'(t_j)}{\sqrt{\Sigma u'^2(t_i)\Sigma u'^2(t_j)}} \tag{2}$$

with k an integer slot number. Ideally, at zero lag-time $\hat{\rho} = 1$; (white) noise causes a lower value in practice, the difference is used to assess the noise contribution Ψ. To segregate periodic flow contributions, van Maanen (1999) proposed fitting the auto-correlation function with a damped cosines, Eq. (3):

$$\hat{\rho}_{fit}(\tau) = b + c_0 e^{-\alpha_0 \tau} + \Sigma_{n=1}^{i} c_n e^{-\alpha_n \tau} \cos(2 \cdot nf\pi\tau) \tag{3}$$

Summing the amplitudes Σc_n then gives the contribution of periodic motions to the fluctuating kinetic energy. Alternatively, the kinetic energy contribution of periodic flow can be estimated from the spectral density function Eq. (4):

$$S(f) = \frac{\Delta t}{\pi}\left[\frac{1}{2}\hat{\rho}(k\Delta\tau_{lag})w(k\Delta\tau_{lag})\cos(kf\Delta\tau_{lag})\right] \tag{4}$$

With w a Tukey–Hanning window (Tummers and Passchier, 1996, 1772c) with width $t_m(f) = t_{max}\kappa f_0/f$, where lower κ decreases low-frequency resolution, but high κ can induce modulation We found $\kappa = 5$ provided a good trade-off. The relative contribution of periodic components follows from integrating Eq. (4) over the relevant frequencies, which was done using trapezoidal integration. With these methods, the RMS velocity $u_{rms} = \sqrt{\bar{u'u'}}$ can be corrected for the periodic components, by Eq. (5) when periodic fitting is used and Eq. (6) when using spectral integration:

$$u'_t = u' \cdot \sqrt{1 - \Psi - \Sigma(c_n)} \tag{5}$$

$$u'_t = u' \cdot \sqrt{1 - \Psi - (E_p/E_t)} \tag{6}$$

Here, E_p/E_t is the fraction of energy contained in the periodic spectral components of u'. We report k_t as the MI-free turbulent kinetic energy based on u'_t, k_{t^*} as the total fluctu-

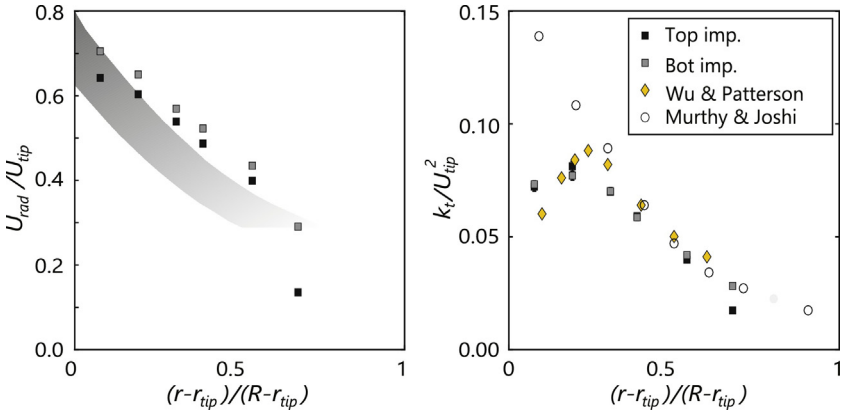

Fig. 2 – LDA results: current data (top and bottom impeller outflow) compared with earlier studies by Wu and Patterson (1989), Murthy and Joshi (2008). The position is scaled with tank and impeller tip radius, U_{rad} and k_t with the tip speed U_{tip}.

ating energy based on u', and k_{MI} as the kinetic energy of macro-instabilities, $k_{t^*} - k_t$. Since the tangential velocity is not measured, isotropy is assumed to yield $k_t = 3/4(\overline{u'^2_{t,ax}} + \overline{u'^2_{t,rad}})$. Experimentally, we use the subscripts *fit* and SI to distinguish between k_t and k_{MI} computed with correlation fitting and spectral integration, respectively. In the impeller outflow $\hat{\rho}$ was evaluated for $\tau_{lag} = 250$ ms with 500 slots, which sufficed to capture noise and blade passages. The well-defined impeller-induced periodicity gave preference to Eq. (5) for periodic estimation, taking the first 3 harmonics into account. In the inter-compartment region, $\hat{\rho}$ was evaluated first for $\tau_{lag} = 250$ ms with 500 slots to estimate noise (no impeller influence was observed), and next at $\tau_{lag} = 40$ s with 1600 slots to evaluate MI-induced periodicity. As a high-resolution, long lag time computation was unfeasible, we estimated the total spectral density function by matching the spectrum of both lag time ranges in the overlapping frequency range to construct a single spectrum. In the inter-compartment region, $\hat{\rho}$ was fitted with 4 cosines, at 2 frequencies ($f_{1.1}$ and $f_{2.1}$) and their first harmonics ($f_{1.2}$ and $f_{2.2}$). Spectral density integration requires a cut-off between turbulent and MI components. We considered the range $f/N < 0.1$ (10 impeller revolutions) as MI-components, based on visual assessment of the spectra. Of course, the cut-off point can be debated, but as we use the same definition between experiment and CFD changing the cut-off should not affect the comparison.

4. Results and discussion

4.1. *Experimental*

4.1.1. *LDA verification*

Ranade and Joshi (1990) compared a range impeller outflow measurements, summarized in the gray band of Fig. 2. Our data coincides with the upper bound, we observe a somewhat slower decline in U_{rad} with radial position. The differences may arise because of variations in signal processing, LDA setup, and sensitivity of U_{rad} to the axial position. The rapid drop at $r = 102$ mm is attributed to the vicinity of the baffle. A good agreement in turbulent kinetic energy k_t is observed compared to Wu and Patterson (1989), Murthy and Joshi (2008) reported a higher k_t near the tip, likely since they measured all three velocity components and avoided the isotropy assumption.

4.1.2. *inter-compartment dynamics*

We now focus on the dynamics in the inter-compartment region. LDA results for this region are presented in Fig. 3, in combination with CFD for MRF–RKE. The CFD results will be discussed later, in Section 4.4.1. It can be observed that U_{rad} exhibits mirror-symmetry in the plane $y = 0$ (Fig. 3A), with some deviations near the baffle, and a decreasing magnitude of U_{rad} nearing the stirrer shaft. The typical flow patterns of disc turbines mean the flow moves towards $y = 0$ in the wall region (convergent pattern), this switches to flow away from $y = 0$ in the center (divergent pattern) between $r/R = 0.694$ and $r/R = 0.566$ (Fig. 3B).

The total fluctuating kinetic energy k_{t^*} reaches a maximum at $y = 0$ at every radial position, except closest to the baffle (Fig. 3C). This peak in k_{t^*} could originate both from MIs and from turbulent kinetic energy generated by the collision of the flow loops of the top- and bottom impeller. To discriminate between these possible origins, the presence of low-frequency periodic components in the LDA signal was assessed by generating the auto-correlation function $\hat{\rho}$ of the signal and fitting with Eq. (3). The fits are visualized in Fig. 4, with the fit parameters given in Table 5.

As noted in Section 3.2.1, two frequencies ($f_{1.1}$ and $f_{2.1}$) and their first harmonics ($f_{1.2}$ and $f_{2.2}$) are fitted. This gives $f_{1.1}/N = 0.020 \pm 0.001$ and $f_{2.1}/N = 0.061 \pm 0.003$ axially, and $f_{1.1}/N = 0.015 \pm 0.007$ and $f_{2.1}/N = 0.052 \pm 0.015$ radially. These values agree well with the precessing vortex and jet instability frequencies as reported by Paglianti et al. (2008). The total MI kinetic energy, $k_{MI,fit}$, reaches a maximum at $y = 0$ at all radial positions. An overview of all fitting results is provided in Table 5.

The radial oscillations are comparatively weak: $\Sigma C_{n,rad} < 0.075$ at all locations except at $r/R = 0.694$. The result at $r/R = 0.694$ is a fitting error, no strong periodic components are observable in Fig. 4, and the damping coefficients a_n (Eq. (3)) are at the constraint value $a_n = 0.33$, indicating a poor fit. Axial oscillations have a higher magnitude; $\Sigma C_{n,ax}$ varies from 0.1 at the shaft to 0.22 at $r/R = 0.694$. Close to the shaft $f_{1.1}$ is twice the strength of its harmonic $f_{1.2}/N = 0.040$. For $r/R > 0.358$, $f_{1.2}/N$ is by far the stronger contribution. Overall, $f_{2.1}/N = 0.061$ has the highest magnitude, exceeding $f_{1.2}/N$ by a factor 1.5 – 2, except at $r/R = 0.2$. The noise component Ψ is around 1–6% at all points, except $r/R = 0.765$. This is consistent at all axial locations; the correlation function shows a much more rapid decay at this position (not shown). We have not been able to pinpoint the exact reason for this higher noise level; it could be that the presence of the baffle leads to relatively dominant small-scale turbulence, meaning the data-rate was insufficient. Furthermore, imperfections in refractive-index matching are most pronounced at this position, and the vicinity of the

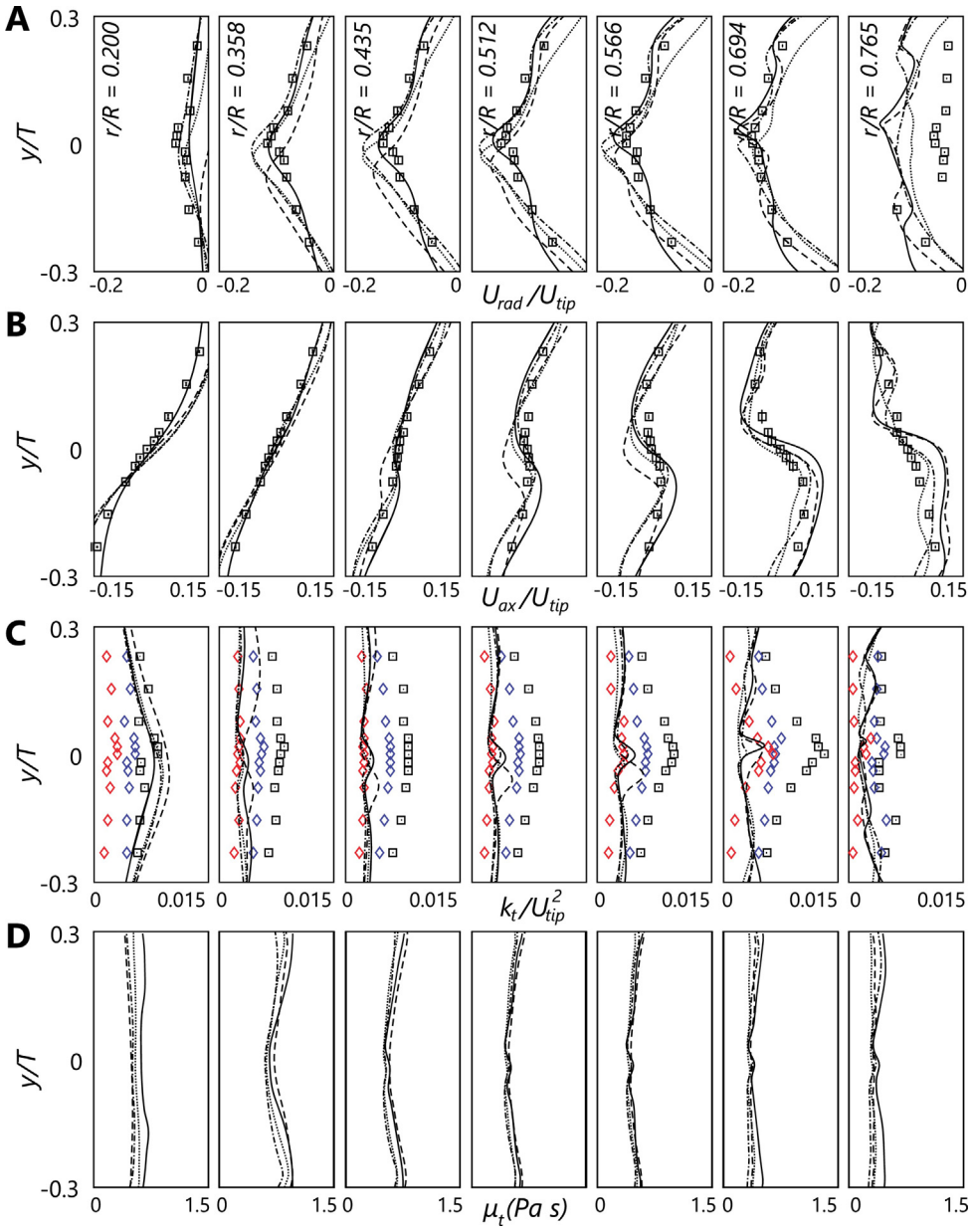

Fig. 3 – Axial profiles (baffle plane) of A: U_{rad}, B: U_{ax}, C: k_t, comparing LDA results (symbols) with CFD data (lines) for MRF–RKE, 360° domain. By construction $k_{MI} = 0$ for MRF simulations, hence $k_t = k_{t^*}$. In fig. C, the black rectangles represent the total kinetic energy k_{t^*}, the blue diamonds the turbulent kinetic energy k_t, and the red diamonds the MI energy k_{MI}. Lines: CFD results at different mesh densities (dotted: 2IF – C, dash-dot: 2IF – M, dashed: 2IF – F, solid: 2IF – SF). Row (D) shows the tangential average of μ_t acquired from the CFD simulations. (For interpretation of the references to color in this legend, the reader is referred to the web version of the article.)

baffle may lead to higher background noise by reflection effects.

The frequencies fitted by Eq. (3) contribute 8–20% to the fluctuating kinetic energy at $y = 0$. MIs have a less well defined frequency than stirrer blade passages, which suggests auto-correlation fitting under-estimates their contribution by excessive dampening and/or missing out additional frequencies. This makes it likely $k_{MI,fit}$ is underestimated by Eq. (5). Using the spectral density function and determining $k_{MI,SI}$ using Eq. (6), the kinetic energy contained in the range $f/N < 0.1$ lies between 28 and 49% at $y = 0$, as reported in Table 6. However, this method does not discriminate MI frequencies from other large-scale contributions, and is considered over-estimative. The non-discriminatory nature of the spectral density method does make comparison with LES spectra more straightforward (part II), as LES simulations showed less well-defined frequencies. Hence, the MI energies reported in the CFD comparison come from the spectral density method, with the notion that the true MI energy is likely to lie in between the estimates of Eqs. (5) and (6). Fig. 5 shows the spectral density function of $\hat{\rho}_{uax}$. In agreement with the auto-correlation fits discussed previously, a clear bi-modal peak representing $f_{1.2}/N$ and $f_{2.1}/N$ is visible, with increasing prominence at the outer radial positions.

Since we are interested in inter-compartment mixing, $u'_{ax,MI}$ is of particular interest; in this direction the jet instability frequency contributes most. Whether MIs will strongly affect mixing depends on whether the observed oscillations represent a cross-flow between the compartments, or the segregation between the compartments moving up and down as a whole. The unsteady CFD results presented in part II of this

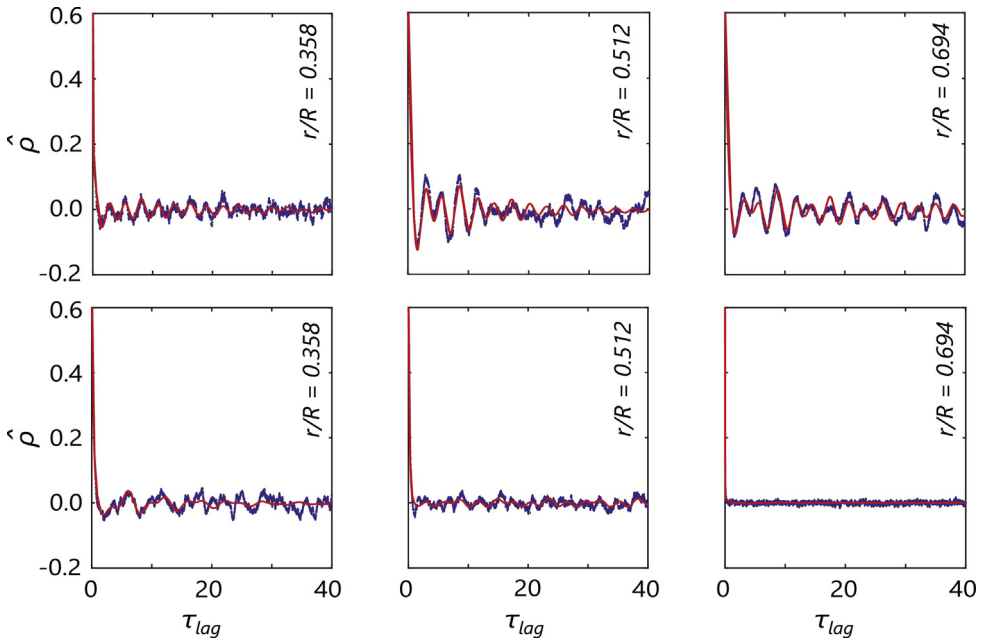

Fig. 4 – Fitted auto-correlation functions of u'_{ax} (top) and u'_{rad} (bottom) at 3 radial locations, in the plane y = 0. Blue: LDA data. Red: fitted function with 4 damped cosines, at 2 base frequencies and their first harmonic. (For interpretation of the references to color in this legend, the reader is referred to the web version of the article.)

Table 5 – RMS-velocity, noise factor Ψ, MI-correction factor, oscillation frequencies and kinetic energy in the plane y = 0 at different radial positions, using the periodic-fitting approach (Eq. (5)). The coefficient c represent the contribution to the Reynolds stress $\overline{u'u'}$, with $c_{i,j}$ the jth harmonic of frequency component i.

r/R	0.200	0.358	0.435	0.512	0.566	0.694	0.765
u'_{rad} (m/s)	0.149	0.135	0.127	0.115	0.107	0.091	0.083
Ψ_{rad}	0.015	0.017	0.022	0.032	0.037	0.064	0.317
$c_{1.1,rad}$	0	0.006	0.016	0.017	0.006	0.032	0.010
$c_{1.2,rad}$	0.037	0.048	0.040	0.007	0.003	0.002	0.001
$c_{2.1,rad}$	0	0.015	0.075	0.009	0.012	0.045	0.006
$c_{2.2,rad}$	0.032	0.005	0.028	0.016	0.011	0.039	0.012
$f_{1.1,rad}/N$	0.020	0.001	0.015	0.015	0.022	0.017	0.017
$f_{2.1,rad}/N$	0.049	0.058	0.056	0.053	0.050	0.043	0.062
u'_{ax} (m/s)	0.082	0.098	0.112	0.134	0.154	0.194	0.151
Ψ_{ax}	0.063	0.054	0.045	0.041	0.033	0.027	0.192
$c_{1.1,ax}$	0.049	0.022	0.029	0.031	0	0	0
$c_{1.2,ax}$	0.022	0.005	0.052	0.095	0.064	0.070	0.055
$c_{2.1,ax}$	0.027	0.044	0.043	0.102	0.113	0.135	0.073
$c_{2.2,ax}$	0.003	0.007	0.009	0.014	0	0.011	0
$f_{1.1,ax}/N$	0.020	0.017	0.021	0.020	0.021	0.020	0.020
$f_{2.1,ax}/N$	0.053	0.062	0.065	0.062	0.062	0.061	0.061
$10^3 \times k_{t,fit}/U_{tip}^2$	7.73	7.63	7.49	7.54	8.85	10.80	6.17
$10^3 \times k_{MI,fit}/U_{tip}^2$	0.62	0.41	0.78	1.36	1.23	2.40	0.70

Table 6 – MI-correction factor and kinetic energy in the plane y = 0 at different radial positions, using the spectral integration approach (Eq. (6)). The RMS velocity and noise factor are as in Table 5.

r/R	0.200	0.2358	0.3435	0.512	0.566	0.694	0.765
$(E_p/E_t)_{rad}$ (Eq. (6))	0.409	0.380	0.337	0.267	0.222	0.140	0.029
$(E_p/E_t)_{ax}$ (Eq. (6))	0.164	0.140	0.200	0.288	0.391	0.546	0.318
$10^3 \cdot k_{t,2}/U_{tip}^2$	5.38	5.57	5.91	6.32	6.60	6.77	4.67
$10^3 \cdot k_{MI,2}/U_{tip}^2$	3.04	2.47	2.35	2.58	3.52	6.45	2.22

paper suggest compartment cross-flow predominantly occurs close to the shaft. However, we first focus on the performance of MRF simulations with steady-state hydrodynamics (frozen flowfield), which are inherently unable to capture MIs by their steady state nature.

4.2. CFD: multiple reference frames

4.2.1. CFD validation: the impeller outflow

Fig. 6 shows U_{rad}, k_t and ϵ in the top impeller outflow (360°, MRF–RKE (top) and MRF–RSM (bottom)). Due to the frozen flow-

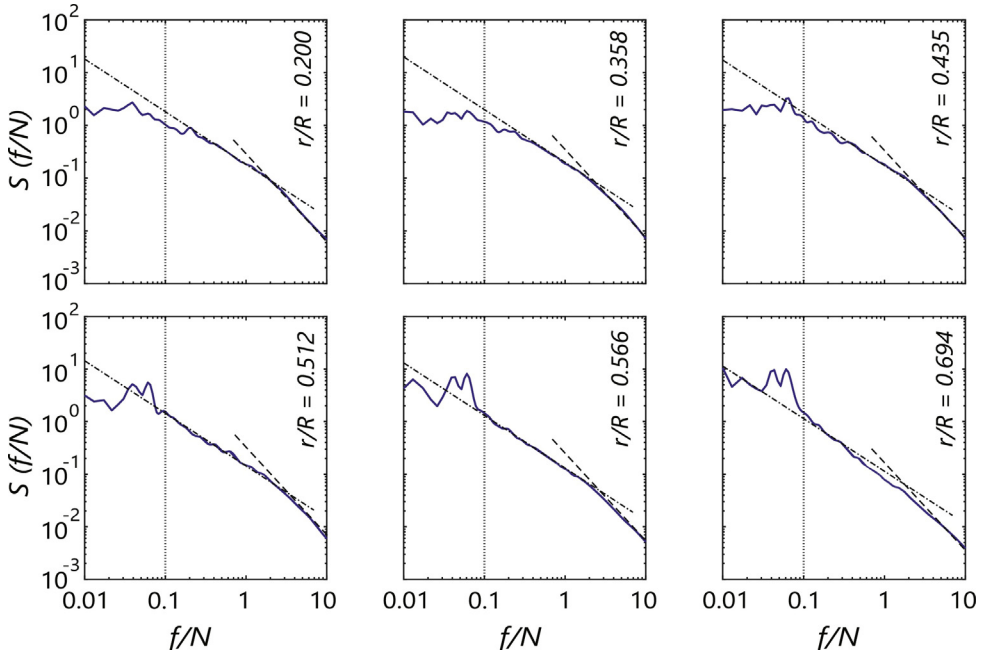

Fig. 5 – Spectral density functions of $\hat{\rho}_{uax}$ at various radial positions and y = 0. Dashed line: $S(f/N) \propto (f/N)^{-5/3}$. Dash-dot line: $S(f/N) \propto (f/N)^{-1}$. Dotted line: cut-off frequency between MI and turbulence.

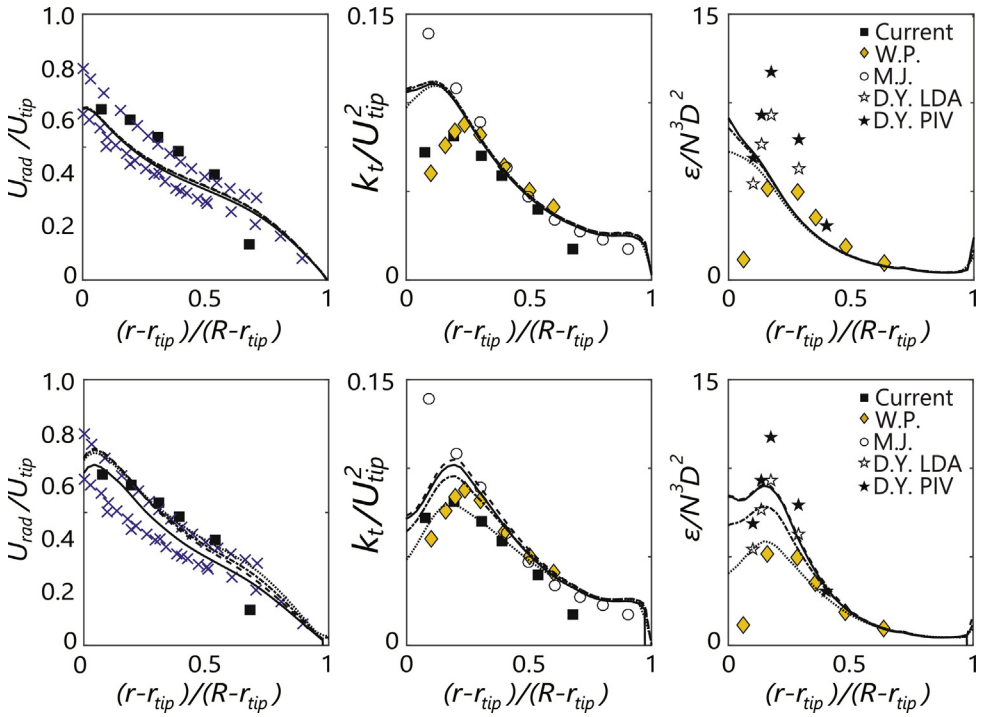

Fig. 6 – Tangentially averaged profiles of U_{rad}, k_t and ϵ in the top impeller outflow compared with phase-averaged LDA data, for MRF simulations. Top row: realizable $k-\epsilon$, 360° domain. Bottom row: RSM 360° domain. Lines represent CFD data; dotted line: 2*IF* – *C*, dash-dot line: 2*IF* – *M*, dashed line: 2*IF* – *F*, solid line: 2*IF* – *SF*. Symbols represent experimental data. Abbreviations: W.P. Wu and Patterson (1989), M.J. Murthy and Joshi (2008), D.Y. Ducci and Yianneskis (2005). The blue crosses in the U_{rad} plot represent the upper- and lower bound of the studies reviewed by Ranade and Joshi (1990). (For interpretation of the references to color in this legend, the reader is referred to the web version of the article.)

field in MRF, $k_{MI} = 0$ by construction, and $k_t = k_{t^*}$. The profiles were tangentially averaged in order account for all impeller angles. In our view, this is a fairer comparison with LDA data than the instantaneous outflow profile directly from the impeller tip, although it reduces agreement near the baffle where the flow is not rotation-dominated. No experimental profiles for ϵ have been reported for the current study, as the equipment did not have sufficient resolution for such measurements.

Both turbulence models predict U_{rad} and k_t well within the LDA data range; k_t does deviate close to the impeller, where the isotropic turbulence assumption breaks down. Interestingly, the non-isotropic RSM predicts a k_t decrease at the tip, which is in better agreement with our data and Wu and Patterson (Wu and Patterson, 1989) than with Murthy and Joshi (Murthy

Table 7 – Comparison of dimensionless mixing times θ_{95} for the MRF method: models and mesh dependency. Methods: P = bottom probe, C = coefficient of mixing. The work of Hartmann is followed to set the CoM-boundary.

Mesh	RKE, bot/top	RKE, CoM	RSM, bot/top	RSM, CoM
2IF-C	**133.5**/110.5	148.5	**138.1**/107.1	152.0
2IF-M	**146.1**/120.0	162.0	**157.8**/127.9	173.0
2IF-F	**145.2**/120.3	160.5	**145.2**/113.1	159.5
2IF-SF	**180.9**/151.4	200.0	n.m.	172.5
2IP-C	**96.2**/n.m.	106.5	**113.0**/*n. m*	129.0
2IP-M	**117.1**/95.0	129.0	**166.4**/*n. m*	161.5
2IP-F	**135.9**/113.1	152.0	**176.5**/*n. m*	161.0

n.m. = not measured.

and Joshi, 2008), while only the latter measured all (fluctuating) velocity components. RSM yields a superior assessment for ϵ; at the highest mesh density the peak dissipation rate recorded by Baldi and Yianneskis (2004), Baldi et al. (2004), Ducci and Yianneskis (2005) is reasonably captured. The RKE model agrees with the dimensional assessment of Wu and Patterson (Wu and Patterson, 1989), likely arising from the similar underlying assumptions. Except for ϵ at the blade tip with $2IF-C$, no mesh dependency is observed in the RKE outflow profiles. The RSM model is more mesh sensitive, but independence is reached with $2IF-F$. Further parameters related to mesh dependence are discussed in Supplementary material B. Based on impeller outflow data, both turbulence models perform satisfactory. Due to similarity the bottom impeller profiles and profiles for the 60° mesh are omitted.

4.3. *Mixing times*

We quantify θ_{95} by two methods; a probe at the same location as used by Jahoda et al. (2007) for direct comparison, and the CoM as used by Hartmann et al. (2006) to quantify mixing in the entire volume. Lacking experimental data for the latter, it is reported for mutual comparison between simulations only. The results are reported in Table 7. Experimentally, Jahoda et al. report a bottom probe mixing time $\theta_{95,bot} = 92$. For their top-probe no mixing time is explicitly reported, $\theta_{95,top} \approx 75$ is estimated from their probe response profiles.

For the 360°-meshes, the probe-based θ_{95} for both RKE and RSM exceeds the experimental for both probes substantially. The over-prediction increases with increasing mesh density, with a factor 2 over-estimation at the finest mesh, while still being possibly mesh-dependent. We consider it unlikely such a degree of over-estimation is a result of the (invasive) probe influencing the flow experimentally, which is supported by similar results between invasive and non-invasive point measurements in single impeller systems (Distelhoff et al., 1997; Javed et al., 2006). Probe readings may be location dependent, implying the concluded over-estimation of θ_{95} may be location-specific. To exclude this, additional probes have been monitored in the bottom compartment, yielding very similar θ_{95}, both for MRF (Supplementary material C) and SM–LES simulations (part II of this study). This is logical consequence of inter-compartment mixing being the rate limiting step, leading to a relatively homogeneous concentration *within* the bottom compartment. The similar θ_{95} between several bottom-compartment probes, combined with the similar degree of over-estimation of θ_{95} by the top- and bottom-probe compared to experimental data, gives confidence the concluded over-estimation in θ_{95} is not an artifact of probe location. Hence, the logical conclusion is that the offset in θ_{95} results from inherent limitations in the modeling approach.

Table 8 – Axial flow-rate Q_{ax} (downward) through the mid-impeller plane y = 0 in L/s. For the 60° mesh, the value is multiplied by 6.

Mesh	RKE 360°	RSM 360°	RKE 60°	RSM 60°
X-C	1.36	1.58	3.04	2.45
X-M	1.14	1.28	2.72	1.34
X-F	1.48	1.31	1.10	2.25
X-SF	0.74	1.46	–	–

We do note some outliers in the CFD results; both for RKE and RSM, τ_{95} deviates from the trend for $2IF-F$. This appears to be a mesh effect, which is further discussed in Section 4.4.1. The 60° mesh yields a systematically lower θ_{95} with RKE. This was not a consequence of the 6-fold symmetry introducing additional injection points, but rather of increased axial exchange between the compartments (see Section 4.4.1). With the RSM model, the 60° mesh yields similar CoM figures as in the 360° mesh, but whereas the CoM becomes constant, the probe value keeps increasing. This does indicate different mixing behavior *within* the compartments for the RSM model.

4.4. *Inter-compartment flow*

4.4.1. *Multiple reference frames*

360° *domain*. The profiles for U_{rad} and U_{ax} compare reasonably well with experimental data using RKE (Fig. 3A and B), although both are over-predicted close to the baffle, probably due to the use of a 2*D* baffle geometry. The change from converging to diverging axial flow is well captured. Some mesh differences can be detected, but aside from $2IF-F$ no mesh performs particularly better or worse.

For $2IF-F$, the peak in U_{rad} and inflection point of U_{ax} lie slightly below y = 0. This indicates the inter-compartment plane has shifted compared to y = 0. In Table 8 we report the integral downward flowrate Q_{ax} at y = 0. The higher this value, the more convective exchange between the stirrer compartments by the mean flow (by mass conservation, the upward flowrate was always equal). Q_{ax} typically decreases with mesh density, but $2IF-F-RKE$ is a clear outlier, which agrees with the shift in U_{rad} and U_{ax} observed in Fig. 3. Taken together, this explains why θ_{95} is comparatively low in $2IF-F$, despite k_t and tangentially-averaged turbulent viscosity $\bar{\mu_t}$ (Fig. 3D) being similar to the other cases: the higher Q_{ax} promotes mixing between the stirrer compartments. Near the shaft, k_t is reasonably captured, but this agreement already breaks down for r/R = 0.358. The peak in k_t at y = 0, most prominent in the converging flow region, is underestimated by about a factor two using RKE; on top of that the energy contained in MIs is not captured by virtue of the steady state nature of MRF simulations. The tangential averages of μ_t, Fig. 3D, show little difference between the meshes; the value for $2IF-SF$ narrowly exceeds the others. This indicates $\bar{\mu_t}$ is not responsible for the increasing θ_{95} upon increasing mesh density. It is, however, likely that $\bar{\mu_t}$ is structurally under-predicted due to the poor assessment of k_t, leading to a structural over-prediction of θ_{95} as Q_{ax} converges to a low, mesh-independent value. It is this trend of decreasing Q_{ax} with an increasing grid resolution that causes the sensitivity θ_{95} to mesh density. Note that an increased Q_{ax} through y = 0 does not necessarily mean

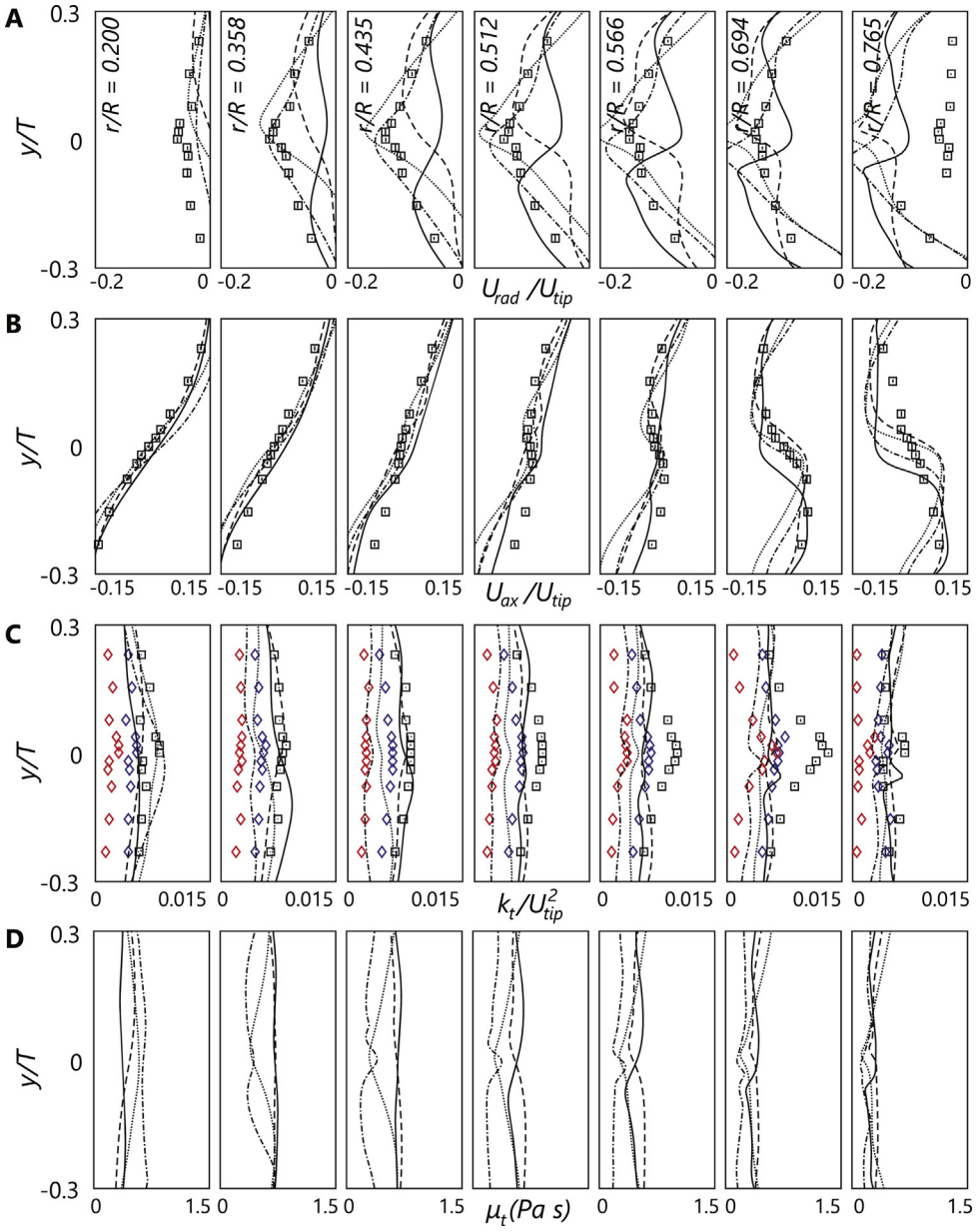

Fig. 7 – Axial profiles (baffle plane) of A: U_{rad}, B: U_{ax}, C: k_t, comparing LDA results (symbols) with CFD data (lines) for MRF–RSM, 360° domain. By construction $k_{MI} = 0$ for MRF simulations, hence $k_t = k_{t^*}$. In fig. C, the black rectangles represent the total kinetic energy k_{t^*}, the blue diamonds the turbulent kinetic energy k_t, and the red diamonds the MI energy k_{MI}. Lines: CFD results at different mesh densities (dotted: 2IF – C, dash-dot: 2IF – M, dashed: 2IF – F, solid: 2IF – SF). Row (D) shows the tangential average of μ_t acquired from the CFD simulations. (For interpretation of the references to color in this legend, the reader is referred to the web version of the article.)

increased exchange between the compartments, as the inter-compartment plane and y = 0 may not exactly overlap, but there does appear to be a correlation between the two. The U_{rad} and U_{ax} profiles for RSM (Fig. 7) are in lesser agreement with experimental data. For 2IF – M the velocity profiles favorably match the LDA measurements, but for both 2IF – F and 2IF – SF the U_{rad} peak shows strange asymmetric behavior. As for the RKE case, the skewed inter-compartment plane increases Q_{ax} in the y = 0 plane (Table 8), explaining why θ_{95} is nearly similar for 2IF – M, 2IF – F and 2IF – SF with MRF–RSM.

60° *domain, MRF* In contrast to the full domain, U_{rad} and U_{ax} are poorly predicted in the 60° domain (Fig. 8, rows A, B). The magnitude of U_{rad} is strongly under-estimated everywhere except close to the baffle, while reversal from converging to diverging axial flow is not at all captured within the measured region. The peak U_{rad} is predicted at a lower axial position than measured experimentally. The MRF–RKE model does yield a comparatively good estimation of k_t for the 2IP – SF mesh, resulting in a higher tangentially averaged μ_t (Fig. 8, row E). Furthermore Q_{ax} is significantly higher in the 60° domain (Table 8). Combined, the high μ_t and axial flowrate explain the low θ_{95} observed for RKE in the 60° domain.

Compared to RKE, RSM shows much more mesh dependency, with unexpected U_{rad} peaks. k_t is reasonably assessed for r/R < 0.5. Overall, μ_t and Q_{ax} are similar between the 360° and 60° domain, explaining the similarity in θ_{95} between them. As was the case with the full-domain, there seems to be a shift in plane position compared to the experimental data for the denser meshes.

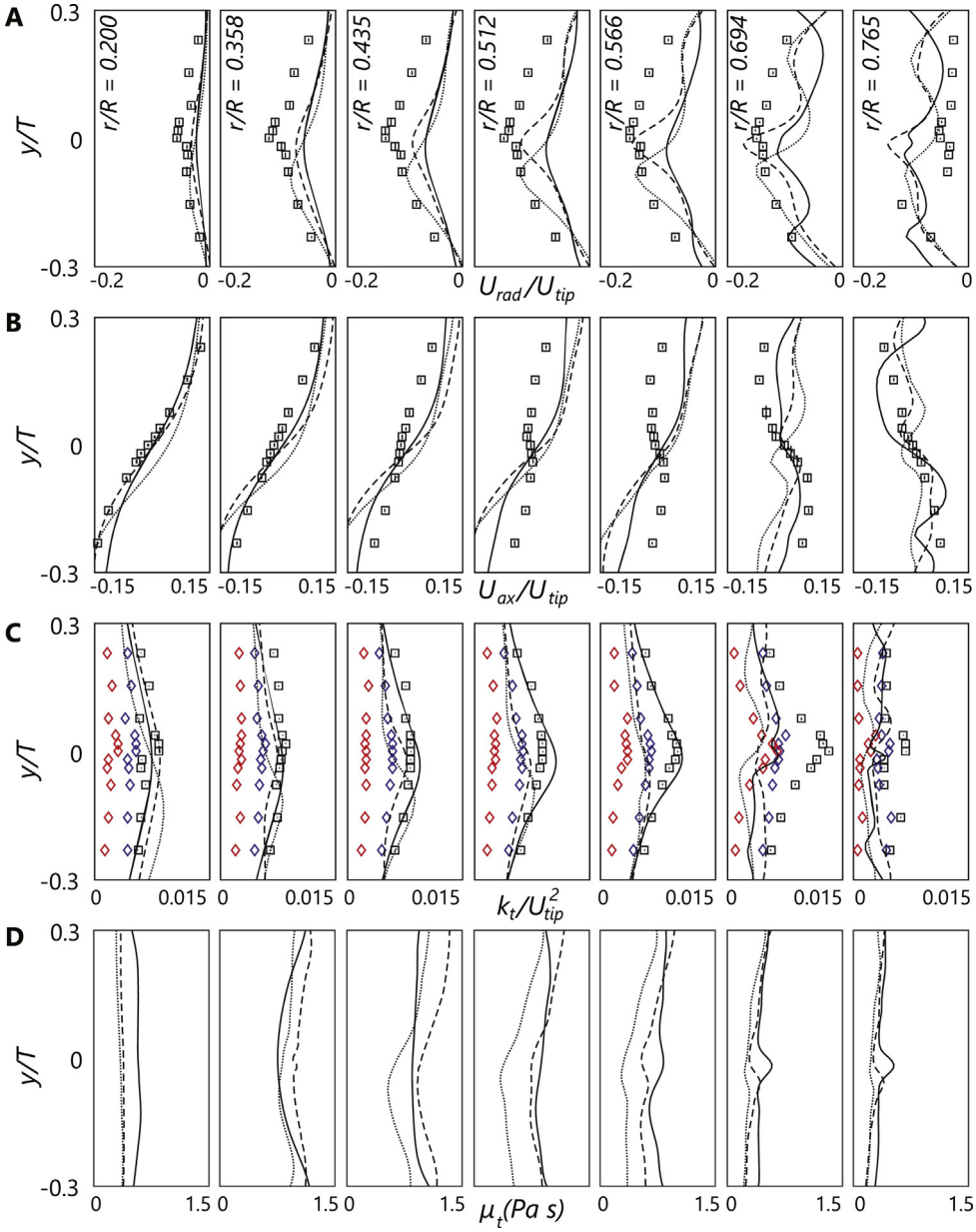

Fig. 8 – Axial profiles (baffle plane) of A: U_{rad}, B: U_{ax}, C: k_t, comparing LDA results (symbols) with CFD data (lines) for MRF–RKE, 60° domain. By construction $k_{MI} = 0$ for MRF simulations, hence $k_t = k_{t^*}$. In fig. C, the black rectangles represent the total kinetic energy k_{t^*}, the blue diamonds the turbulent kinetic energy k_t, and the red diamonds the MI energy k_{MI}. Lines: CFD results at different mesh densities (dotted: 2IF – C, dash-dot: 2IF – M, dashed: 2IF – F, solid: 2IF – SF). Row (D) shows the tangential average of μ_t acquired from the CFD simulations. (For interpretation of the references to color in this legend, the reader is referred to the web version of the article.)

5. Concluding remarks

Multi-Rushton stirred tanks are prone to compartment formation around the impellers, with inter-compartment transfer becoming the rate limiting factor for mixing. The mixing time θ_{95} appears to depend strongly on 2 factors: turbulent exchange between the compartments, and the effect of macro-instabilities (MIs) on inter-compartment dynamics. Using LDA, we find evidence of MIs at $f/N = 0.020$ and $f/N = 0.062$, which are in agreement with earlier reported values for the precessing vortex and jet instability (Paglianti et al., 2006, 2008). Depending on the method of estimation, the MIs contain at between 15% (from auto-correlation) and 30% (from spectral integration) of the total fluctuating kinetic energy k_{t^*}, although close to the baffle this may be as high as 20–50%, most significantly in the axial direction. This makes it likely that MIs have a considerable effect on mass transfer between the compartments.

Multiple reference frame (MRF) CFD modeling has been employed in prior literature to multi-impeller stirred tanks, exploiting its steady-state nature to reduce computation time. A literature analysis revealed that (1) θ_{95} typically increased with mesh density, (2) the simulations reported in literature were unlikely mesh-independent, and (3) mesh-independent results are expected to over-predict θ_{95} strongly. Our own MRF simulations, focused on the inter-compartment region, confirms the increasing over-predictions of θ_{95} with increasing mesh density. A significant under-estimation of k_{t^*} in the inter-compartment region is observed. In part this is due to the complete absence of macro-instabilities in steady-state MRF simulations, but also the predicted turbulent kinetic

energy k_t is lower than the LDA measurements; this is attributed to Reynolds-averaged MRF simulations predicting a largely shear-free inter-compartment plane, leading to an under-prediction in the generation of k_t by the colliding compartment flow-loops. The turbulent viscosity μ_t in the inter-compartment region, which via the turbulent Schmidt number Sc_t controls turbulent mixing, is nearly independent of mesh density. While the inherent over-prediction of θ_{95} may be attributed to the under-predicted k_{t^*}, via an under-estimated μ_t), the increasing θ_{95} with mesh density has another origin. It was found that, despite the radial flow in the inter-compartment plane, the axial flowrate Q_{ax} through the horizontal plane $y = 0$ is not exactly 0, inducing some convective axial mixing. This Q_{ax} reduced with increasing mesh resolution, corresponding to the increasing θ_{95}. There were some outliers where a comparatively low θ_{95} and high Q_{ax} was observed; further scrutiny revealed the inter-compartment plane was slightly tilted inter-compartment plane was predicted here. This implies the presence of MIs allows some ambiguity in the inter-compartment plane position predicted in steady-state MRF, which can make the simulations highly sensitive to the mesh layout and initial conditions. In this study we exclusively made use of structured hexahedral meshes. With tetrahedral meshes, a higher degree of numerical diffusion may also lower θ_{95}. In the limit of $N_c \to \infty$, strong over-predictions of θ_{95} are still expected, regardless of the mesh type. Using a 60° section of the domain yielded good flow agreement in the impeller region, but very poor agreement in the inter-compartment region. Typically, Q_{ax} was higher yielding lower θ_{95}, but not as a result of better flow prediction. More likely, forcing the inherently unstable segregation plane into 6-fold periodicity introduces artificial axial exchange. This means the assumption of periodicity should be avoided in multi-impeller mixing studies, not because it artificially multiplies feedpoints, but because it poorly captures flow between the compartments. To conclude, the MRF model is not able to assess the relevant dynamics for mixing in multi-Rushton tanks, and quite likely so in other cases where compartmentalized flow is observed. Tuning of Sc_t is sometimes proposed in literature to improve agreement in θ_{95}. This ad-hoc solution is likely to negatively impact intra-compartment mixing, which does appear to be assessed properly, judging from single-impeller mixing simulations (Coroneo et al., 2011). Furthermore, the exact Sc_t correction depends on the strength of MIs, the degree of underestimation of μ_t, and the predicted position of the inter-compartment plane, which may all vary on a case-by-case basis, thereby losing predictive value. In applications where transient methods mixing simulations are computationally unfeasible, and crude agreement in mixing behavior suffices, Sc_t tuning may be tolerable, but the limitations of the MRF model must be kept in mind. For detailed mixing studies, such as the quantitative assessment of impeller configurations in multi-impeller mixing tanks, the observed limitations make the MRF model with a frozen flow-field inherently unsuitable. In the second part of this work, we will discuss how sliding mesh RANS and LES perform in this respect.

Acknowledgements

We wish to thank our colleagues at ECUST, Shanghai and DSM Sinochem pharmaceuticals for our ongoing collaboration. We are grateful to Prof. H. van den Akker, Dr. S. Kenjeres, Dr. L. Portela and Prof. H.J. Noorman for their advice and insights. CH acknowledges all students following MSc course CH3421, who contributed to the simulation results as part of their course reports. Evert Wagner, Jos Thieme, Christiaan Schinkel, Stefan ten Hagen, Youp van Goozen and Ruud van Tol are gratefully acknowledged for their technical assistance. This work has been conducted within a multi-party research project, between DSM-Sinochem Pharmaceuticals, TU Delft, East China University of Science and Technology and Guojia, subsidized by NWO and MoST (NWO-MoST Joint program 2013DFG32630). All sponsors are gratefully acknowledged.

Appendix A. Supplementary data

Supplementary data associated with this article can be found, in the online version, at https://doi.org/10.1016/j.cherd.2018.06.005.

References

Ammar, M., Chtourou, W., Driss, Z., Abid, M., 2011. Numerical investigation of turbulent flow generated in baffled stirred vessels equipped with three different turbines in one and two-stage system. Energy 36 (8), 5081–5093, http://dx.doi.org/10.1016/j.energy.2011.06.002.

Baldi, S., Yianneskis, M., 2004. On the quantification of energy dissipation in the impeller stream of a stirred vessel from fluctuating velocity gradient measurements. Chem. Eng. Sci. 59 (13), 2659–2671, http://dx.doi.org/10.1016/j.ces.2004.03.021.

Baldi, S., Ducci, A., Yianneskis, M., 2004. Determination of dissipation rate in stirred vessels through direct measurement of fluctuating velocity gradients. Chem. Eng. Technol. 27 (3), 275–281, http://dx.doi.org/10.1002/ceat.200401979.

Brucato, A., Ciofalo, M., Grisafi, F., Micale, G., 1998. Numerical prediction of flow fields in baffled stirred vessels: a comparison of alternative modelling approaches. Chem. Eng. Sci. 53 (21), 3653–3684, http://dx.doi.org/10.1016/S0009-2509(98)00149-3.

Bujalski, W., Jaworski, Z., Nienow, A., 2002a. CFD study of homogenization with dual Rushton turbines-comparison with experimental results. Chem. Eng. Res. Des. 80 (1), 97–104, http://dx.doi.org/10.1205/026387602753393402.

Bujalski, J., Jaworski, Z., Bujalski, W., Nienow, A., 2002b. The influence of the addition position of a tracer on CFD simulated mixing times in a vessel agitated by a Rushton turbine. Chem. Eng. Res. Des. 80 (8), 824–831, http://dx.doi.org/10.1205/026387602321143354.

Bujalski, W., Jaworski, Z., Nienow, A., 2002c. CFD study of homogenization with dual Rushton turbines – comparison with experimental results: Part II. The multiple reference frame. Chem. Eng. Res. Des. 80 (1), 97–104, http://dx.doi.org/10.1205/026387602753393402.

Coroneo, M., Montante, G., Paglianti, A., Magelli, F., 2011. CFD prediction of fluid flow and mixing in stirred tanks: numerical issues about the RANS simulations. Comput. Chem. Eng. 35 (10), 1959–1968, http://dx.doi.org/10.1016/j.compchemeng.2010.12.007.

Delafosse, A., Collignon, M.-L., Calvo, S., Delvigne, F., Crine, M., Thonart, P., Toye, D., 2014. CFD-based compartment model for description of mixing in bioreactors. Chem. Eng. Sci. 106, 76–85.

Derksen, J., Doelman, M., Van den Akker, H., 1999. Three-dimensional LDA measurements in the impeller region of a turbulently stirred tank. Exp. Fluids 27 (6), 522–532, http://dx.doi.org/10.1007/s003480050376.

Distelhoff, M.F.W., Marquis, A.J., Nouri, J.M., Whitelaw, J.H., 1997. Scalar mixing measurements in batch operated stirred tanks. Can. J. Chem. Eng. 75 (4), 641–652, http://dx.doi.org/10.1002/cjce.5450750401.

Ducci, A., Yianneskis, M., 2005. Direct determination of energy dissipation in stirred vessels with two-point LDA. AIChE J. 51 (8), 2133–2149, http://dx.doi.org/10.1002/aic.10468.
Escudié, R., Liné, A., 2003. Experimental analysis of hydrodynamics in a radially agitated tank. AIChE J. 49 (3), 585–603, http://dx.doi.org/10.1002/aic.690490306.
Escudié, R., Bouyer, D., Liné, A., 2004. Characterization of trailing vortices generated by a Rushton turbine. AIChE J. 50 (1), 75–86, http://dx.doi.org/10.1002/aic.10007.
Guillard, F., Trägårdh, C., Fuchs, L., 2000a. A study of turbulent mixing in a turbine-agitated tank using a fluorescence technique. Exp. Fluids 28 (3), 225–235, http://dx.doi.org/10.1007/s003480050382.
Guillard, F., Trägårdh, C., Fuchs, L., 2000b. New image analysis methods for the study of mixing patterns in stirred tanks. Can. J. Chem. Eng. 78 (2), 273–285, http://dx.doi.org/10.1002/cjce.5450780201.
Gunyol, O., Mudde, R.F., 2009. Computational study of hydrodynamics of a standard stirred tank reactor and a large-scale multi-impeller fermenter. Int. J. Multiscale Comput. Eng. 7 (6), 559–576.
Gunyol, O., Noorman, H.J., Mudde, R.F., 2009. CFD simulations of a large-scale fermenter with multiple impellers. In: Chaouki, P., Tanguy, J. (Eds.), Proceedings of the 9th International Conference on Gas–Liquid Solid Reactor Engineering. Montreal, pp. 1–4.
Haringa, C., Tang, W., Deshmukh, A.T., Xia, J., Reuss, M., Heijnen, J.J., Mudde, R.F., Noorman, H.J., 2016. Euler–Lagrange computational fluid dynamics for (bio)reactor scale down: an analysis of organism lifelines. Eng. Life Sci. 16 (7), 652–663, http://dx.doi.org/10.1002/elsc.201600061.
Haringa, C., Deshmukh, A.T., Mudde, R.F., Noorman, H.J., 2017. Euler–Lagrange analysis towards representative down-scaling of a 22m3 aerobic *S. cerevisiae* fermentation. Chem. Eng. Sci. 170, 653–669, http://dx.doi.org/10.1016/j.ces.2017.01.014.
Hartmann, H., Derksen, J., Montavon, C., Pearson, J., Hamill, I., van den Akker, H., 2004. Assessment of large eddy and RANS stirred tank simulations by means of LDA. Chem. Eng. Sci. 59 (12), 2419–2432, http://dx.doi.org/10.1016/j.ces.2004.01.065.
Hartmann, H., Derksen, J.J., van den Akker, H.E.A., 2006. Mixing times in a turbulent stirred tank by means of LES. AIChE J. 52 (11), 3696–3706, http://dx.doi.org/10.1002/aic.10997.
Huchet, F., Linë, A., Morchain, J., 2009. Evaluation of local kinetic energy dissipation rate in the impeller stream of a Rushton turbine by time-resolved PIV. Chem. Eng. Res. Des. 87 (4), 369–376, http://dx.doi.org/10.1016/J.CHERD.2008.11.012.
Jahoda, M., Machon, V., 1994. Homogenization of liquids in tanks stirred by multiple impellers. Chem. Eng. Technol. 17 (2), 95–101, http://dx.doi.org/10.1002/ceat.270170205.
Jahoda, M., Moštěk, M., Kukuková, A., Machon, V., 2007. CFD modelling of liquid homogenization in stirred tanks with one and two impellers using large eddy simulation. Chem. Eng. Res. Des. 85 (5), 616–625, http://dx.doi.org/10.1205/cherd06183.
Javed, K., Mahmud, T., Zhu, J., 2006. Numerical simulation of turbulent batch mixing in a vessel agitated by a Rushton turbine. Chem. Eng. Process. Process Intensif. 45 (2), 99–112, http://dx.doi.org/10.1016/j.cep.2005.06.006.
Jaworski, Z., Bujalski, W., Otomo, N., Nienow, A., 2000a. CFD study of homogenization with dual Rushton turbines – comparison with experimental results. Chem. Eng. Res. Des. 78 (3), 327–333, http://dx.doi.org/10.1205/026387600527437.
Jaworski, Z., Bujalski, W., Otomo, N., Nienow, A., 2000b. CFD study of homogenization with dual Rushton turbines – comparison with experimental results: Part I. Initial studies. Chem. Eng. Res. Des. 78 (3), 327–333, http://dx.doi.org/10.1205/026387600527437.
Jenne, M., Reuss, M., 1999. A critical assessment on the use of $k-\epsilon$ turbulence models for simulation of the turbulent liquid flow induced by a Rushton-turbine in baffled stirred-tank reactors. Chem. Eng. Sci. 54 (17), 3921–3941, http://dx.doi.org/10.1016/S0009-2509(99)00093-7.
Khopkar, A., Aubin, J., Rubio-Atoche, C., Xuereb, C., Le Sauze, N., Bertrand, J., Ranade, V.V., 2004. Flow generated by radial flow impellers: PIV measurements and CFD simulations. Int. J. Chem. React. Eng. 2 (1), http://dx.doi.org/10.2202/1542-6580.1146.
Kukuková, A., Moštěk, M., Jahoda, M., Machon, V., 2005. CFD prediction of flow and homogenization in a stirred vessel: Part I. Vessel with one and two impellers. Chem. Eng. Technol. 28 (10), 1125–1133, http://dx.doi.org/10.1002/ceat.200500094.
Kukuková, A., Noël, B., Kresta, S.M., Aubin, J., 2008. Impact of sampling method and scale on the measurement of mixing and the coefficient of variance. AIChE J. 54 (12), 3068–3083, http://dx.doi.org/10.1002/aic.11639.
Kukukova, A., Aubin, J., Kresta, S.M., 2009. A new definition of mixing and segregation: three dimensions of a key process variable. Chem. Eng. Res. Des. 87 (4), 633–647, http://dx.doi.org/10.1016/j.cherd.2009.01.001.
Lane, G.L., Schwarz, M.P., Evans, G.M., 2000. Comparison of CFD methods for modeling stirred tanks. In: Proc. 10th European Conference on Mixing (Delft), Vol. 5805, Elsevier.
Lee, K., Yianneskis, M., 1997. A liquid crystal thermographic technique for the measurement of mixing characteristics in stirred vessels. Chem. Eng. Res. Des. 75 (8), 746–754, http://dx.doi.org/10.1205/026387697524416.
Lee, K.C., Yianneskis, M., 1998. Turbulence properties of the impeller stream of a Rushton turbine. AIChE J. 44 (1), 13–24, http://dx.doi.org/10.1002/aic.690440104.
Liné, A., Gabelle, J.-C., Morchain, J., Anne-Archard, D., Augier, F., 2013. On POD analysis of PIV measurements applied to mixing in a stirred vessel with a shear thinning fluid. Chem. Eng. Res. Des. 91 (11), 2073–2083, http://dx.doi.org/10.1016/j.cherd.2013.05.002.
Magelli, F., Montante, G., Pinelli, D., Paglianti, A., 2013. Mixing time in high aspect ratio vessels stirred with multiple impellers. Chem. Eng. Sci. 101, 712–720, http://dx.doi.org/10.1016/j.ces.2013.07.022.
Micale, G., Brucato, A., Grisafi, F., Ciofalo, M., 1999. Prediction of flow fields in a dual-impeller stirred vessel. AIChE J. 45 (3), 445–464, http://dx.doi.org/10.1002/aic.690450303.
Mishra, V.P., Joshi, J.B., 1994. Flow generated by a disc turbine: Part IV. Multiple impellers. Chem. Eng. Res. Des. 72, 657–668.
Moštěk, M., Kukuková, A., Jahoda, M., Machon, V., 2005. CFD prediction of flow and homogenization in a stirred vessel: Part II. Vessel with three and four impellers. Chem. Eng. Technol. 28 (10), 1134–1143, http://dx.doi.org/10.1002/ceat.200500093.
Montante, G., Moštěk, M., Jahoda, M., Magelli, F., 2005. CFD simulations and experimental validation of homogenisation curves and mixing time in stirred Newtonian and pseudoplastic liquids. Chem. Eng. Sci. 60 (8-9), 2427–2437, http://dx.doi.org/10.1016/j.ces.2004.11.020.
Moo-Young, M., Tichar, K., Dullien, F.A.L., 1972. The blending efficiencies of some impellers in batch mixing. AIChE J. 18 (1), 178–182, http://dx.doi.org/10.1002/aic.690180133.
Murthy, B., Joshi, J., 2008. Assessment of standard, RSM and LES turbulence models in a baffled stirred vessel agitated by various impeller designs. Chem. Eng. Sci. 63 (22), 5468–5495, http://dx.doi.org/10.1016/j.ces.2008.06.019.
Nere, N.K., Patwardhan, A.W., Joshi, J.B., 2003. Liquid-phase mixing in stirred vessels: turbulent flow regime. Ind. Eng. Chem. Res. 42 (12), 2261–2698, http://dx.doi.org/10.1021/IE0206397.
Ng, K., Yianneskis, M., 2000. Observations on the distribution of energy dissipation in stirred vessels. Chem. Eng. Res. Des. 78 (3), 334–341, http://dx.doi.org/10.1205/026387600527446.
Ng, K., Fentiman, N., Lee, K., Yianneskis, M., 1998. Assessment of sliding mesh CFD predictions and LDA measurements of the flow in a tank stirred by a Rushton impeller. Chem. Eng. Res. Des. 76 (6), 737–747, http://dx.doi.org/10.1205/026387698525315.
Nienow, A., 1997. On impeller circulation and mixing effectiveness in the turbulent flow regime. Chem. Eng. Sci. 52 (15), 2557–2565, http://dx.doi.org/10.1016/S0009-2509(97)00072-9.
Nikiforaki, L., Montante, G., Lee, K., Yianneskis, M., 2003. On the origin, frequency and magnitude of macro-instabilities of the

flows in stirred vessels. Chem. Eng. Sci. 58 (13), 2937–2949, http://dx.doi.org/10.1016/S0009-2509(03)00152-0.
Nikiforaki, L., Yu, J., Baldi, S., Genenger, B., Lee, K., Durst, F., Yianneskis, M., 2004. On the variation of precessional flow instabilities with operational parameters in stirred vessels. Chem. Eng. J. 102 (3), 217–231, http://dx.doi.org/10.1016/j.cej.2004.05.002.
Paglianti, A., Montante, G., Magelli, F., 2006. Novel experiments and a mechanistic model for macroinstabilities in stirred tanks. AIChE J. 52 (2), 426–437, http://dx.doi.org/10.1002/aic.10634.
Paglianti, A., Liu, Z., Montante, G., Magelli, F., 2008. Effect of macroinstabilities in single- and multiple-impeller stirred tanks. Ind. Eng. Chem. Res. 47 (14), 4944–4952, http://dx.doi.org/10.1021/ie800253u.
Raghav Rao, K.S.M.S., Joshi, J.B., 1988. Joshi, liquid phase mixing in mechanically agitated vessels. Chem. Eng. Commun. 74 (1), 1–25, http://dx.doi.org/10.1080/00986448808940445.
Ranade, V.V., Joshi, J.B., 1990. Flow generated by a disc turbine: II. Mathematical modelling and comparison with experimental data. Chem. Eng. Res. Des. 68 (1), 34–50, URL http://cat.inist.fr/?aModele=afficheN&cpsidt=6817059.
Ranade, V., Perrard, M., Le Sauze, N., Xuereb, C., Bertrand, J., 2001. Trailing vortices of Rushton turbine: PIV measurements and CFD simulations with snapshot approach. Chem. Eng. Res. Des. 79 (1), 3–12, http://dx.doi.org/10.1205/026387601528471.
Rewatkar, V., Joshi, J.B., 1991. Effect of impeller design on liquid phase mixing in mechanically agitated reactors. Chem. Eng. Commun. 102 (1), 1–33, http://dx.doi.org/10.1080/00986449108910846.
Roussinova, V., Kresta, S.M., Weetman, R., 2003. Low frequency macroinstabilities in a stirred tank: scale-up and prediction based on large eddy simulations. Chem. Eng. Sci. 58 (11), 2297–2311, http://dx.doi.org/10.1016/S0009-2509(03)00097-6.
Rutherford, K., Lee, K.C., Mahmoudi, S.M.S., Yianneskis, M., 1996. Hydrodynamic characteristics of dual Rushton impeller stirred vessels. AIChE J. 42 (2), 332–346, http://dx.doi.org/10.1002/aic.690420204.
Schäfer, M., Höfken, M., Durst, F., 1997. Detailed LDV measurements for visualization of the flow field within a stirred-tank reactor equipped with a Rushton turbine. Chem. Eng. Res. Des. 75 (8), 729–736, http://dx.doi.org/10.1205/026387697524399.
Singh, H., Fletcher, D.F., Nijdam, J.J., 2011. An assessment of different turbulence models for predicting flow in a baffled tank stirred with a Rushton turbine. Chem. Eng. Sci. 66 (23), 5976–5988, http://dx.doi.org/10.1016/j.ces.2011.08.018.
Tominaga, Y., Stathopoulos, T., 2007. Turbulent Schmidt numbers for CFD analysis with various types of flowfield. Atmos. Environ. 41 (37), 8091–8099, http://dx.doi.org/10.1016/j.atmosenv.2007.06.054.
Tummers, M.J., Passchier, D.M., 2001. Spectral analysis of biased LDA data. Meas. Sci. Technol. 12 (10), 1641–1650, http://dx.doi.org/10.1088/0957-0233/12/10/304.
Tummers, M.J., Passchier, D.M., 1996. Spectral estimation using a variable window and the slotting technique with local normalization. Meas. Sci. Technol. 7 (11), 1541–1546, http://dx.doi.org/10.1088/0957-0233/7/11/001.
van Maanen, H.R.E., Nobach, H., Benedict, L.H., 1999. Improved estimator for the slotted autocorrelation function of randomly sampled LDA data. Meas. Sci. Technol. 10 (1), L4–L7, http://dx.doi.org/10.1088/0957-0233/10/1/002.
van Maanen, H.R.E., 1999. Retrieval of Turbulence and Turbulence Properties from Randomly Sampled Laser-Doppler Anemometry Data with Noise (PhD Thesis). Delft University of Technology, URL http://www.anemo.nl/dissertations/Dissertation-H.R.E._van_Maanen.pdf.
Venneker, B.C., Derksen, J.J., Van den Akker, H.E., 2010. Turbulent flow of shear-thinning liquids in stirred tanks – the effects of Reynolds number and flow index. Chem. Eng. Res. Des. 88 (7), 827–843, http://dx.doi.org/10.1016/j.cherd.2010.01.002.
Wu, H., Patterson, G., 1989. Laser-Doppler measurements of turbulent-flow parameters in a stirred mixer. Chem. Eng. Sci. 44 (10), 2207–2221, http://dx.doi.org/10.1016/0009-2509(89)85155-3.
Yeoh, S., Papadakis, G., Yianneskis, M., 2005. Determination of mixing time and degree of homogeneity in stirred vessels with large eddy simulation. Chem. Eng. Sci. 60 (8-9), 2293–2302, http://dx.doi.org/10.1016/j.ces.2004.10.048.
Zadghaffari, R., Moghaddas, J., Revstedt, J., 2010. Large-eddy simulation of turbulent flow in a stirred tank driven by a Rushton turbine. Comput. Fluids 39 (7), 1183–1190, http://dx.doi.org/10.1016/j.compfluid.2010.03.001.
Zakrzewska, B., Jaworski, Z., 2004. CFD modeling of turbulent jacket heat transfer in a Rushton turbine stirred vessel. Chem. Eng. Technol. 27 (3), 237–242, http://dx.doi.org/10.1002/ceat.200401988.